EUROFUSION WPJET1-PR(16) 14450

C Paz-Soldan et al.

The non-thermal origin of the tokamak low-density stability limit

Preprint of Paper to be submitted for publication in
Nuclear Fusion

This work has been carried out within the framework of the EUROfusion Consortium and has received funding from the Euratom research and training programme 2014-2018 under grant agreement No 633053. The views and opinions expressed herein do not necessarily reflect those of the European Commission.

The non-thermal origin of the tokamak low-density stability limit

C. Paz-Soldan,[1, a)] R. J. La Haye,[1] D. Shiraki,[2] R. J. Buttery,[1] N.W. Eidietis,[1] E.M. Hollmann,[3] R.A. Moyer,[3] J.E. Boom,[4] I.T. Chapman,[5] and JET Contributors[6]

[1)] *General Atomics, San Diego, California, 92121, USA*
[2)] *Oak Ridge National Laboratory, Oak Ridge, Tennessee, 37831, USA*
[3)] *University of California-San Diego, La Jolla, CA, 92093, USA*
[4)] *Max-Planck-Institut fur Plasmaphysik, Boltzmannstrasse 2, D-85748 Garching, Germany*
[5)] *CCFE, Culham Science Centre, Abingdon, Oxon, OX14 3DB, UK*
[6)] *EUROfusion Consortium, JET, Culham Science Centre, Abingdon,OX14 3DB, UK, See the appendix of Romanelli F. et al., (2014 Proc. of the 25th IAEA Fusion Energy Conf. (Saint Petersburg, Russia))*

(Dated: 10 November 2015)

DIII-D plasmas at very low density exhibit onset of n=1 error field (EF) penetration (the 'low-density locked mode') not at a critical density or EF, but instead at a critical level of runaway electron (RE) intensity. Raising the density during a discharge does not avoid EF penetration, so long as RE growth proceeds to the critical level. Penetration is preceded by non-thermalization of the electron cyclotron emission, anisotropization of the total pressure, synchrotron emission shape changes, as well as decreases in the loop voltage and bulk thermal electron temperature. The same phenomena occur despite various types of optimal EF correction, and in some cases modes are born rotating. Similar phenomena are also found at the low-density limit in JET. These results stand in contrast to the conventional interpretation of the low-density stability limit as being due to residual EFs and demonstrate a new pathway to EF penetration instability due to REs. Existing scaling laws for penetration project to increasing EF sensitivity as bulk temperatures decrease, though other possible mechanisms include classical tearing instability, thermo-resistive instability, and pressure-anisotropy driven instability. Regardless of first-principles mechanism, known scaling laws for Ohmic energy confinement combined with theoretical RE production rates allow rough extrapolation of the RE criticality condition, and thus the low-density limit, to other tokamaks. The extrapolated low-density limit by this pathway decreases with increasing machine size and is considerably below expected operating conditions for ITER. While likely unimportant for ITER, this mechanism can explain the low-density limit of existing tokamaks operating with small residual EFs.

I. INTRODUCTION AND OBSERVATION

The low-density tokamak stability limit is conventionally believed to be related to the magnitude of residual error fields (EFs), with the limiting instability being n=1 EF penetration at the $q = 2$ rational surface forming a laboratory frame tearing mode. This instability is commonly referred to as the low-density locked mode, and is disruptive at sufficiently low edge safety factor (≈ 3). Empirical scaling studies were conducted on multiple tokamaks to find the parametric dependency of the EF penetration limit on engineering parameters such as density, toroidal field, safety factor, and major radius.[1–7] A robust experimental result is that the density at penetration (n_{LM}) is linearly proportional to the applied or residual n=1 EF magnitude (δB_{crit}). These scalings have in turn been the subject of sustained theoretical interest.[8–13]

Implicit in the linear scaling with density is the absence of a low-density limit. Both experimental scalings and theoretical analysis agree that as EF magnitude is brought towards zero, vanishingly low-density operation should be possible. In contrast, experiments find that even with very accurate EF correction, EF penetration is still found at a finite density. This has been conventionally attributed to the presence of higher-order EFs that were not correctable using n=1 coilsets with fixed poloidal spectra, such as n>1 EFs or poloidal sidebands of the n=1 EF.[3,14–16] While n>1 may still play a role, the residual n=1 EF hypothesis stands in contrast to modern understanding of EF correction for low-density access,[17,18] where EF penetration sensitivity is found to be dominantly to a single (correctable) n=1 EF component.

An effect that becomes important at low density (yet is not considered in the conventional picture) is the phenomenon of thermal runaway, also called Dreicer generation.[19–21] This effect populates the low-density tokamak discharge with an increasingly large number of runaway electrons (REs). This effect was recognized in early explorations of tokamak operating space, with some 'Hugill' diagrams indicating a boundary to normal operation (but not a stability limit) at low density due to REs.[22,23]

This work will present observations to illustrate that REs set the low-density stability limit in present tokamaks, and not residual uncorrected EFs. While the limiting instability is still n=1 EF penetration, the impact of

[a)] Electronic mail: paz-soldan@fusion.gat.com

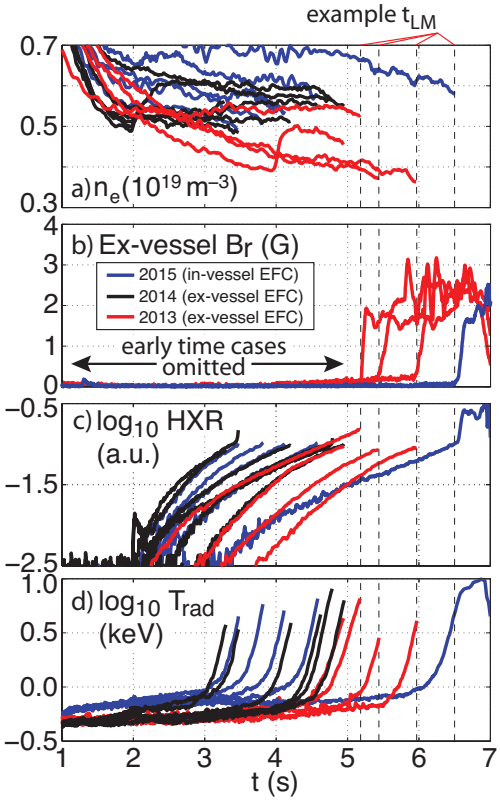

FIG. 1. Low-density stability limit discharges on DIII-D from multiple years, with most traces truncated for clarity at the moment of EF penetration (t_{LM}). Despite (a) various levels of line-average density (n_e), radial field penetration (b) is preceded by gradual RE growth as observed on (c) HXR detectors, followed by (d) sharp increase of ECE radiation temperature approximately 250 ms prior to penetration. I_p flat-top is at 0.8 s for these discharges.

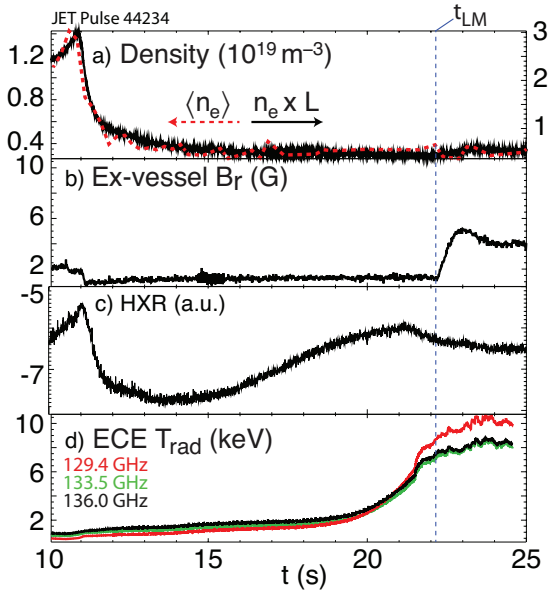

FIG. 2. Low density stability limit observed on JET. An extended period (5 s) at low yet nearly constant (a) density eventually yields penetration, evidenced by (b) ex-vessel B_r measurements. As with DIII-D, penetration is preceded by a gradual increase in (c) HXR emission followed by a sharp increase in (d) the ECE emission indicating non-thermalization of the emission. I_p flat-top is at 13 s for this discharge.

the REs on the bulk thermal population will be demonstrated to drive instability. Several first-principles mechanisms for instability are proposed, and a scaling law is developed to extrapolate the instability onset condition to other devices. While this work is focused on DIII-D data, JET data is also presented to demonstrate operational limits consistent with this picture, as well as to demonstrate that this phenomenology is not peculiar to one tokamak.

Experiments conducted at DIII-D find that despite various types of optimized EF correction, operation below densities of $\approx 5 \times 10^{18}$ m^{-3} robustly yields instability to EF penetration. These are also the densities at which REs are robustly excited by the Dreicer mechanism. Unexpectedly, EF penetration in these discharges occurs at similar levels of RE emission intensity observed in hard X-ray (HXR) and electron cyclotron emission (ECE). This is shown in Fig. 1 for a collection of discharges pushing low density operation for RE dissipation studies.[24] At varying levels of density [Fig. 1(a)], penetration [Fig. 1(b)] is robustly preceded by a gradual rise in HXR emission [$>$ 1 MeV, Fig. 1(c)] followed by a prompt rise in ECE [Fig. 1(d)] about 250 ms prior to instability. As will be shown, penetration is also preceded by a decrease in the loop voltage and thermal electron temperature, anisotropization of the total pressure, and sometimes the appearance of new structures in synchrotron emission images. The aforementioned phenomenology is found to occur even if gas puffing raises the density, so long as RE growth proceeds.

Similar phenomena are observed at the low-density stability limit in JET discharges, shown in Fig. 2. Identified from Fig. 5 of Ref. 3, an extended period at very low (yet nearly constant) density is observed [Fig. 2(a)] prior to penetration. This is conducive to a buildup of RE population as REs will be sourced throughout this phase, and is consistent with a gradual rise in HXR emission [$>$ 0.1 MeV, Fig. 2(c)]. Also consistent with this, ECE signals [Fig. 2(d)] gradually rise throughout the low density phase. Note that these discharges operate with carefully optimized EF correction to enable low-density access, as in DIII-D. The sharp increase of ECE emission beginning well prior to penetration is also observed on JET, suggestive of a similar mechanism. Interestingly, in addition to the HXR and ECE increases, the JET data also show a decrease in HXR emission $\approx$ 1 s before penetration and a discontinuity in ECE $\approx$ 0.5 s before penetration. On DIII-D the HXR decreases only after the penetration and the ECE discontinuity is concurrent with penetration.

These observations will be expanded on in the remainder of this paper, which is structured as follows. The well-known theory of RE growth at low density is briefly reviewed in Sec. II. DIII-D and JET low density operational space is discussed in Sec. III. The phenomenology of the low-density instability is discussed in Sec. IV, and the impact of RE growth discussed in Sec. V. Direct mechanisms for instability are proposed in Sec. VI. Scaling of the low-density limit to existing and future devices is discussed in Sec. VII. Finally, concluding remarks are presented in Sec. VIII.

II. THEORY OF RE GROWTH AT LOW DENSITY

The theory of RE growth in low-density tokamak discharges is well known, with a combination of primary thermal runaway due to the Dreicer effect and secondary avalanche both contributing.[19–21] The initial RE growth is dominated by the Dreicer process, with avalanche multiplication becoming important on the longer time-scale of several multiplication times (> 1 s for these plasmas). For conciseness, the avalanche is not explicitly discussed in this work, though it can be considered as in Ref. 24.

Dreicer generation occurs when the collisional drag on an electron is exceeded by the electric field acceleration.[19,20] The thermal electron-electron collisional frequency is given by $\hat{\nu}_{ee} = n_e e^4 \ln\Lambda/(4\pi\varepsilon_0^2 m_e^2 v_{T_e}^3)$, where n_e is the electron density, $v_{T_e} = \sqrt{2T_e/m_e}$ is the electron thermal speed, T_e is the electron temperature, and $\ln\Lambda$ is the Coulomb logarithm. The electric field E at which an electron traveling at v_{T_e} will runaway is given by the Dreicer field:

$$E_D = \frac{n_e e^3 \ln\Lambda}{4\pi\varepsilon_0^2 T_e}, \tag{1}$$

which is where the acceleration force (eE_D) equals the drag force ($m_e\hat{\nu}_{ee}v_{T_e}$). RE growth by the Dreicer mechanism depends only on the properties of the thermal bulk, and the production rate is given below, in units $[m^{-3}s^{-1}]$:

$$S_{\rm pri} = k n_e \hat{\nu}_{ee} \epsilon_D^{-\frac{3}{16}(1+Z_{\rm eff})} \exp\left(-\tfrac{1}{4}\epsilon_D^{-1} - (1+Z_{\rm eff})^{\frac{1}{2}}\epsilon_D^{-\frac{1}{2}}\right) \exp\left(-\frac{T_e}{m_e c^2}\left[\tfrac{1}{8}\epsilon_D^{-2} + \tfrac{2}{3}(1+Z_{\rm eff})^{\frac{1}{2}}\epsilon_D^{-\frac{3}{2}}\right]\right) \tag{2}$$

where in the above equations $\epsilon_D \equiv E/E_D$ is the normalized electric field, $k = 0.21 + 0.11Z_{\rm eff}$ is an order unity correction with $Z_{\rm eff}$ the effective ion charge,[25] $\varphi = 1 - 1.46(r/R_0)^{\frac{1}{2}} + 1.72(r/R_0)$ is a neoclassical correction factor, and $\tau = (c/v_{T_e})^3\hat{\nu}_{ee}^{-1}$ is the RE collision time.

Dreicer growth is extremely sensitive to E/E_D and thus $V_{\rm loop}$, n_e, and T_e, as has been previously demonstrated both experimentally and theoretically.[24,26] This can be seen in Fig. 3, where the calculated contours of $S_{\rm pri}$ (Eq. 2) are shown in T_e and n_e parameter space. Note that evaluation of $V_{\rm loop}$ on the same parameter space is needed to calculate $S_{\rm pri}$ for Fig. 3. This was scaled from experimental values according to the Spitzer resisitivity scaling ($V_{\rm loop} \propto T_e^{-\frac{3}{2}}$). Also overlayed are the measured evolution of two discharges, which show 3-4 orders of magnitude difference in $S_{\rm pri}$ despite only modestly different n_e. Experimentally, the lower n_e discharge demonstrated strong RE emission while the higher density discharge contained no measurable REs. The extreme sensitivity of Eq. 2 to E/E_D and thus n_e is the essence of extrapolating the low-density limit, and will be revisited in Sec. VII when scaling to other devices.

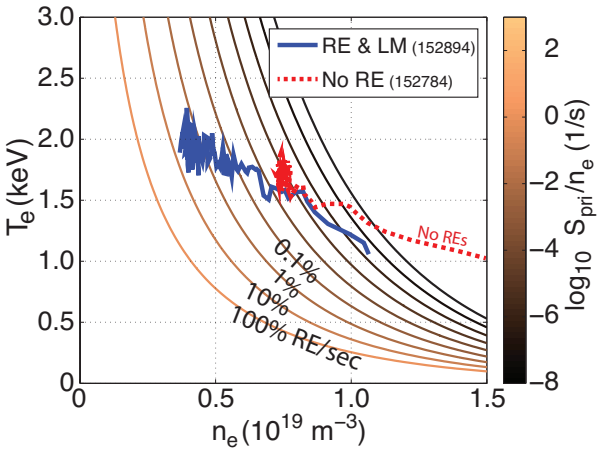

FIG. 3. Evaluation of $S_{\rm pri}$ (Eq. 2) normalized to n_e as a function of n_e and T_e, scaling $V_{\rm loop} \propto T_e^{-3/2}$, showing extreme sensitivity to these parameters. Also included are experimental trajectories of a discharge with robust REs measured, and one with no measurable REs.

III. LOW-DENSITY OPERATIONAL SPACE

In DIII-D and JET accessing the low density regime necessary to observe this instability mechanism is dependent upon accurate correction of intrinsic EFs, as shown in Fig. 4. For both machines, the density at which penetration is observed ($n_{\rm LM}$) is plotted against n=1 correction current (I_C) minus the 'optimal' currents ($I_{\rm opt}$) found through the 'compass scan' technique.[27] For the plasmas considered here, $I_{\rm opt} \approx 0.5$ kA for both machines. Thus, discharges with optimal EF correction lie near $|I_C - I_{\rm opt}| \approx 0$ kA, while discharges with no EF correction lie at $I_C = 0$ and $|I_C - I_{\rm opt}| \approx 0.5$ kA. The difference $I_C - I_{\rm opt}$ is linearly proportional to the residual n=1 EF capable of driving penetration.[17] Indeed a linear scaling of $n_{\rm LM}$ with residual EF is found for discharges at higher n_e without RE populations (black squares).

Interestingly on DIII-D extrapolation of the no-RE points (though sparse) to zero n=1 residual EF ($\mathbf{I}_{\rm opt}$=$\mathbf{I}_C$) does not yield zero $n_{\rm LM}$, indicating residual EFs are impacting the no-RE points. This suggests that if RE production were somehow prevented, EF penetration

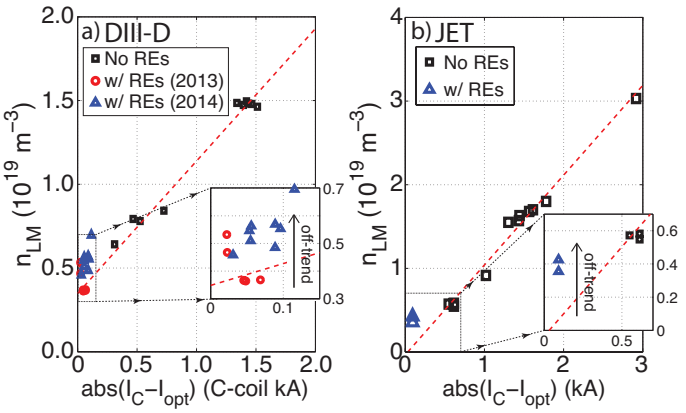

FIG. 4. Density at penetration ($n_{\rm LM}$) vs. n=1 residual EF magnitude for (a) DIII-D and (b) JET. While a linear trend is observed at high density (without REs), at the lowest density instability is observed above the extrapolation from the no RE points. For DIII-D only datapoints with ex-vessel EFC are plotted, while JET points are from an in-vessel coil scan. A subset of this JET data is found in Fig 6 of Ref. 3.

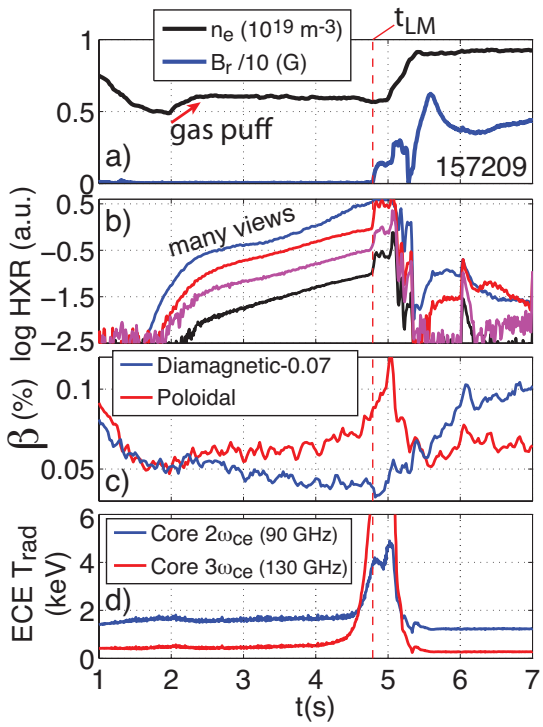

FIG. 5. Detail of a discharge exhibiting low-density limit instability. (a) Density and ex-vessel B_r, showing penetration at $t_{\rm LM}$ despite increase of density at 2 s. (b) Many HXR views at different toroidal and poloidal locations, showing gradual RE emission growth. (c) Divergence between poloidal and diamagnetic β, indicating increasing pressure anisotropy. (d) Sharp increase in ECE radiation temperature in the core and and at high frequency.

through the conventional mechanism may still prevent low-density access even at $\mathbf{I}_{\rm opt}$=$\mathbf{I}_C$ (the compass scan centroid) on DIII-D. While the reason for this elevated extrapolated density limit is not known, it is speculated that $n > 1$ EFs may be responsible. Significant $n > 1$ EFs have been measured on DIII-D in recent experiments[28] and are not affected by n=1 EF correction, potentially allowing penetration of any residual n=1 EF at elevated density through increased rotation braking. This offset density is not evident, however, in scalings found in JET [Fig. 4(b)]. The extrapolated $n_{\rm LM}$ here is found to be very nearly zero.

At the lowest densities in both devices, EF penetration events occur off-trend at $n_{\rm LM}$ above that expected by the no-RE extrapolations (see Fig. 4 insets). These off-trend points contain REs and exhibit the unique phenomenology previewed in Figs. 1 & 2 that are the subject of this work and are now discussed in detail for DIII-D cases.

IV. PHENOMENOLOGY OF LOW-DENSITY STABILITY LIMIT

The phenomenology of the low-density stability limit will now be presented in more detail, first for a single discharge and then for an ensemble of discharges. Figure 5 displays the evolution of key parameters as RE growth proceeds throughout the discharge flat-top. This discharge is selected because it displays a key feature of this mechanism - raising the density does not avoid instability, as would be expected based on conventional scalings. Figure 5(a) shows the n_e trajectory reaching a minimum at 2 s, causing robust RE HXR emission growth [Fig 5(b)], but no penetration [B_r zero in Fig 5(a)]. After raising the density modestly, RE growth proceeds (more slowly), until penetration is found at ≈5 s. Instability onset is observed as a very clear increase in n=1 B_r outside the vessel [Fig 5(a)], and severe disturbances to HXR emission due to RE-wall impacts in the torn magnetic topology. Another phenomenon observed is a divergence of the poloidal and diamagnetic β [Fig 5(c)]. This divergence indicates a significant pressure anisotropy, as $\beta_{\rm pol} = 2\mu_0 \langle p \rangle / B_{\theta a}^2$ is obtained from external magnetics equilibrium reconstructions (EFIT) and $\beta_{\rm dia} = 2\mu_0 \langle p_\perp \rangle / B_{\theta a}^2$ is essentially a scaled measurement from a diamagnetic loop.[29] This will be further discussed shortly.

Finally, ECE emission dramatically increases preceding instability onset [Fig 5(d)]. Emission sensitive to both 2nd and 3rd harmonic of the cyclotron frequency registers the significant increase, and examination of the full ECE spectrum from 100-300 GHz with a Michelson interferometer reveals the spectrum becomes flatter in frequency, increasing most dramatically at high frequency. No obvious features or periodicity in ω_{ce} seen above $3\omega_{ce}$ (130 GHz). Crucially, while other RE measurements increase slowly, this measurement shows a sharp and prompt in-

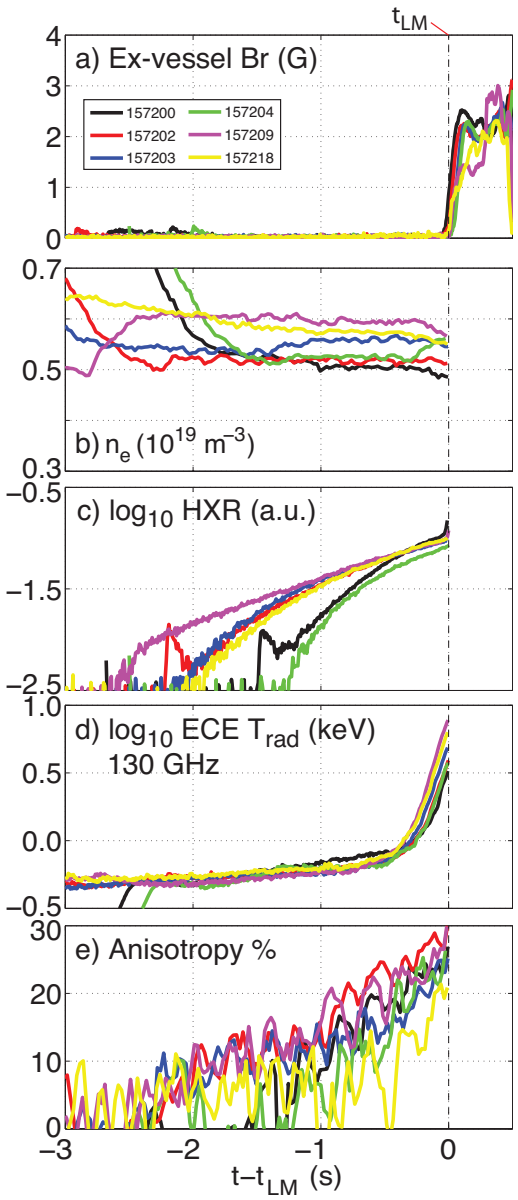

FIG. 6. Summary of phenomena as $t_{\rm LM}$ is approached. (a) Time-base is shifted by $t_{\rm LM}$ across many discharges, with large B_r indicating EF penetration has occured. (b) Instability occurs for a range of n_e, with increasing n_e unable to prevent the mode. (c) While HXR growth begins at different times depending on the n_e trajectory, instability is found at comparable HXR intensity. (d) A sharp rise in ECE emission is also found at a consistent time prior to penetration. (e) Pressure anisotropy also gradually builds with RE population.

crease about 250 ms prior to instability onset. This is a hallmark feature of this phenomenon, and is observed in all cases as was previewed in Fig. 1(c).

While Fig. 5 details a single discharge, the same phenomena are observed in all discharges approaching low density with sufficiently good EF correction. This is shown for a group of discharges in Fig. 6, demonstrating that with time-base shifting by the time of instability ($t_{\rm LM}$), a unification of several RE intensity metrics is found at $t_{\rm LM}$. By definition, Fig. 6(a) verifies that B_r signals exhibit the significant increase corresponding to mode formation and field penetration through the vacuum vessel. This occurs at various levels of density [Fig. 6(b)], and indeed many individual discharges access lower density earlier in the discharge while RE intensity is low, as in Fig. 5. Shifting the time base by $t_{\rm LM}$ aligns RE intensity metrics, such as the HXR emission [Fig. 6(c)], which gradually grows by nearly 2 orders of magnitude during the preceding evolution, and the high-frequency ECE emission [Fig. 6(d)], which demonstrates the hallmark prompt increase prior to $t_{\rm LM}$. While discharges from the same day are chosen to allow direct comparison of HXR intensities (no detector degradation), the same phenomenon is present across many years, as shown in Fig. 1.

The divergence of the diamagnetic and poloidal β shown in Fig. 5(c) is also repeatable across many discharges. This divergence allows a simple estimate of the pressure anisotropy, as $\beta_{\rm pol} \propto \langle p \rangle$ and $\beta_{\rm dia} \propto \langle p_\perp \rangle$. To obtain a pressure anisotropy from the RE beam $\beta_{\rm pol}$ and $\beta_{\rm dia}$, a constant number is first subtracted from $\beta_{\rm dia}$ such that both overlay prior to RE onset [ex. 1.5 s in Fig. 5(c)]. Any subsequent divergence after RE onset (denoted $\Delta_{\rm RE}$) yields a measure of pressure anisotropy by taking $\Delta_{\rm RE}(\beta_{\rm pol} - \beta_{\rm dia}) = 2\mu_0 \langle p_{||,{\rm RE}} \rangle / B_{\theta a}^2$. The pressure anisotropy can then be estimated as $\Delta_{\rm RE}(\beta_{\rm pol} - \beta_{\rm dia})/(\beta_{\rm pol}) \approx \langle p_{||,{\rm RE}} \rangle / \langle p \rangle$. This is plotted in Fig. 6(e), and demonstrates that instability onset occurs at a critical pressure anisotropy as well as HXR and ECE intensity.

Another phenomenon associated with the approach to instability is a modification of the synchrotron emission shape as observed with visible imaging.[30] As shown in Fig. 7, at approximately the time of the ECE divergence a second 'crescent' appears. This second crescent is markedly nearer to the plasma core than the usual crescent observed during stable low-density discharges (Fig. 7(a), and also Fig. 13 of Ref. 24). As synchrotron emission is extremely sensitive to RE pitch angle, any change of this parameter for the core population as anisotropy builds could explain the observation. However, this structure sometimes dies away prior to instability, [as in Fig. 7(c)], while other times it persists to $t_{\rm LM}$. The interpretation or importance of this second structure is not clear, but it is presented for completeness.

Unlike typical static EF penetration, mode onset is sometimes observed in a rotating frame of reference. The mode is not born locked, as can be seen for example in Fig. 8 displaying ECE and magnetics on the low-field side midplane. This particular discharge occurred immediately after optimization of the intrinsic EF correction through the 'compass scan' without changing the plasma conditions, thus employs very accurate EF correction. This discharge also exhibits the other hallmark phenomenology shown in Fig. 6, though it is not plotted.

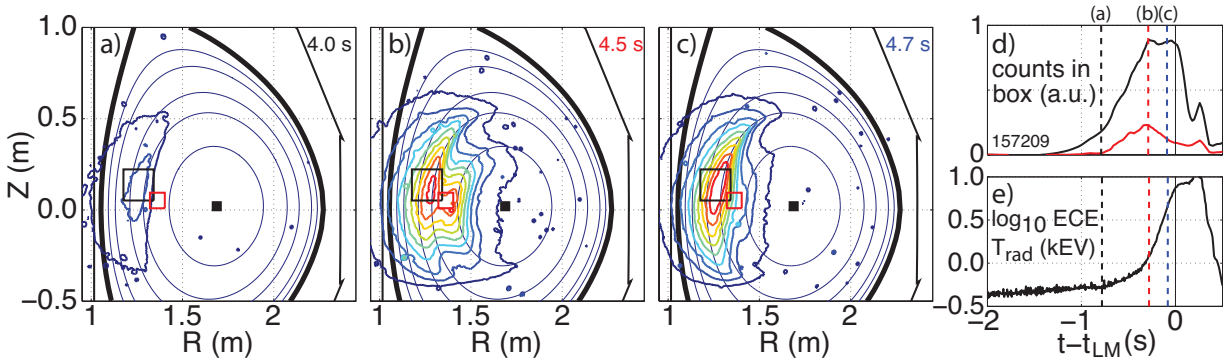

FIG. 7. Evolution of RE synchrotron emission for the discharge of Fig. 5. The generic shape associated with the quiescent low density REs (a) is modified during the sharp ECE rise to include (b) a second structure towards the core. In some but not all discharges the structure subsides prior to penetration, as in (c). Time-histories of (d) counts in sample boxes for each structure and (e) ECE are also included. (e) contains the same data as Fig. 5(d).

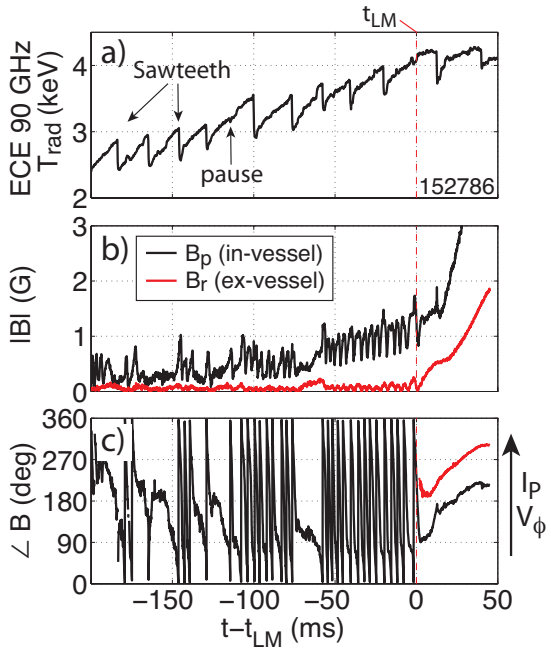

FIG. 8. Onset of low-density locked mode with rotating precursor. (a) Sawtooth oscillations visible on core ECE generate n=1 post-cursor magnetic oscillations, plotted as (b) magnitude and (c) toroidal phase of n=1 field in two components on the LFS midplane. Plasma current (I_p) and impurity toroidal rotation (V_ϕ) direction are indicated. The post-cursor oscillations exist throughout the discharge but transition to the larger mode that soon locks and grows significantly.

Mode onset in this case is difficult to distinguish from sawtooth post-cursor activity, which is always present in these discharges. At 120ms prior to $t_{\rm LM}$, a pause in the sawtooth cycle appears to coincide with the emergence of a more pronounced n=1 rotating mode that continues to grow, before being temporarily locked and unlocked with the sawtooth cycle, until finally it locks permamently and grows to large amplitude at $t_{\rm LM}$. The dynamics are complex, but indicate that the residual EF is not directly driving the low-density instability in this discharge. However, the instability may still be due to penetration of non-axisymmetric fields driven by the sawtooth oscillation. Note rotation profiles measured in similar discharges indicate very little differential rotation is present, allowing core instabilities to couple effectively to the $q = 2$ surface where penetration occurs.

In the majority of cases, however, mode onset is in the laboratory frame and without the clear oscillations that are shown in Fig. 8. For example, instability onset was in the laboratory frame for the discharge of Fig. 5, with the n=1 field growing monotonically as in a traditional EF penetration event. As will be discussed in Sec. VI, these born-locked cases suggest a modification of the sensitivity to EF penetration, as opposed to a new instability mechanism, while the born-rotating cases maintain this possibility.

V. THERMAL EQUILIBRIUM IMPACT OF RE GROWTH

The impact of RE growth on the underlying equilibrium is now discussed. Section II provided the theory needed for a simple estimation of RE current ($I_{\rm RE}$), since REs travel essentially at the speed of light (c), $I_{\rm RE} \approx n_{\rm RE}(\pi r^2 ec)$, where r is the radius of the RE beam with uniform RE density $n_{\rm RE}$ inside. Integrating Eq. 2 and including avalanche multiplication, in an equivalent manner as was done in Ref. 24, the RE current can be estimated and is shown in Fig. 9(a), using a beam minor radius estimate of 25 cm (about half the plasma minor radius). Near the point of instability onset the computed $I_{\rm RE}$ is significant and approaches 10% of the total current ($I_{\rm tot}$). In these discharges the total current is feedback controlled with the loop voltage, thus as $I_{\rm RE}$ approaches $I_{\rm tot}$ a drop in $V_{\rm loop}$ needed to sustain $I_{\rm tot}$ (by a factor $1-I_{\rm RE}/I_{\rm tot}$) is expected, and observed in Fig.

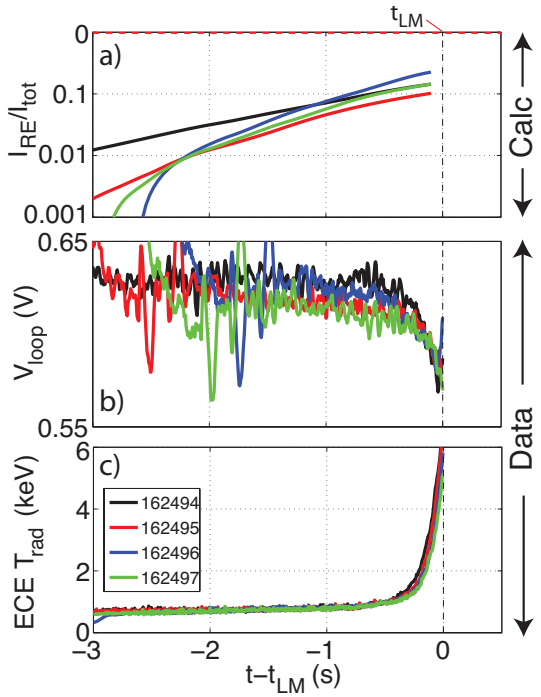

FIG. 9. (a) Calculated RE currents ($I_{\rm RE}$ approaching $t_{\rm LM}$, normalized to total current ($I_{\rm tot}$ = 0.8 MA). (b) Measured $V_{\rm loop}$ begins to decrease as $t_{\rm LM}$ is approached, indicating $I_{\rm RE}$ is becoming significant. (c) All other phenomenon are similar to Fig. 6, including the ECE non-thermalization which diverges on a similar time-scale.

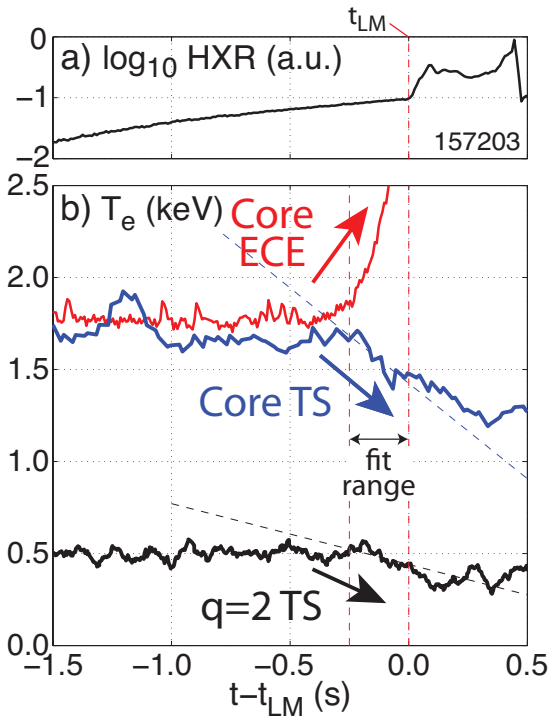

FIG. 10. T_e divergence prior to penetration. While HXR growth (a) and RE pressure (b) is slow, about 250 ms prior to $t_{\rm LM}$ the ECE measurement diverges from Thomson scattering (c). While the effect is more dramatic at the core it also extends to the q=2 surface.

9(b). This is because the REs are nearly collisionless thus have nearly no resistivity, and become essentially a non-inductive current. The effect on $V_{\rm loop}$ occurs promptly, with similar time dependence to the non-thermal ECE signal, shown in Fig. 9(c) for reference.

A consequence of $I_{\rm RE}$ approaching $I_{\rm tot}$ and concomitant reduction of $V_{\rm loop}$ is a reduction in heating power, which in these plasmas with no auxiliary heating is the Ohmic power, equal to $(I_{\rm tot}-I_{\rm RE})V_{\rm loop}$. Note the drop in Ohmic power is quadratic in $I_{\rm RE}$ while the $V_{\rm loop}$ drop is only linear. An expected consequence of a loss in Ohmic power is a reduction of the T_e of the bulk plasma. This is observed promptly prior to instability onset, and is shown in Fig. 10. While HXR (and computed $I_{\rm RE}$) growth is gradual [Fig. 10(a)], the drop in T_e is more prompt, occurring on the time scale of the ECE rise and $V_{\rm loop}$ drop. Note the energy confinement time (τ_E) is only $\approx$ 30 ms in these plasmas. In fact, as can be seen, T_e as measured by two independent diagnostics severely diverges - the ECE measurement rises sharply due to non-thermal emission, while the Thomson scattering (TS) diagnostic registers a drop. This drop is most pronounced in the core (presumably where the RE number and current density is largest) though some drop at the $q = 2$ surface is also observed. Note that it is assumed that the non-thermal component does not affect the analysis of Thomson scattering data. Thus, the impact of increasing $I_{\rm RE}$ can be summarized as a drop in effective resistivity, leading to reduced $V_{\rm loop}$ and thus Ohmic heating. Reduced heating in turn causes a decrease in T_e on a similar timescale to the $V_{\rm loop}$ drop and ECE rise.

VI. CANDIDATE MECHANISMS OF INSTABILITY

Results presented in Secs. IV & V illustrate the emergence of a critical level of RE intensity prior to instability. The critical level is set by when the REs begin to have a significant impact on the bulk thermal equilibrium, leading the plasma to n=1 EF penetration (tearing) instability. However, an actual first-principles mechanism for the penetration of the residual EF and destabilization of the tearing mode has not been identified. A few candidate first-principles mechanisms are presented below, beginning first with consideration of the conventional scaling relationships of EF penetration through torque balance loss. Progressively more speculative mechanisms are then presented, which could be consistent with experimental observations but require further study to be isolated.

$\delta B_{\rm crit}$ Scaling	Dimensionless	Kinetic	T_e	T_eT_i
Visco-Resistive (1993)[8]	$\beta^{-\frac{1}{6}}\nu_*^{\frac{1}{6}}\rho_*^{\frac{4}{3}}$	$T_e^{-\frac{1}{2}}T_i^{\frac{2}{3}}$	-0.5	0.166
Scoville et al. (2003)[9]	$\omega_0\tau_A\left(\frac{\tau_{\rm rec}}{\tau_V}\right)^{\frac{1}{2}}$	$n_e^{\frac{1}{10}}T_e^{\frac{19}{20}}T_i^{-\frac{1}{4}}$	0.95	0.7
Linear-Drift (2006)[10]	$\nu_*^{\frac{1}{4}}\rho_*^{\frac{5}{4}}$	$n_e^{\frac{1}{4}}T_e^{-\frac{1}{2}}T_i^{\frac{5}{8}}$	-0.5	0.125
NTV (2008)[11]	$\beta\nu_*^{-\frac{1}{2}}\rho_*^{\frac{3}{2}}$	$n_e^{\frac{1}{2}}T_e^2T_i^{\frac{3}{4}}$	2	2.75
Rutherford (2012)[12]	$\beta\nu_*^{-1}\rho_*^2$	$T_e^3T_i$	3	4
Polarization(2012)[12]	$\beta\rho_*$	$n_eT_eT_i^{\frac{1}{2}}$	1	1.5

TABLE I. Scaling of EF penetration thresholds with non-dimensional and kinetic parameters in various models. Recent scalings indicate increasing sensitivity as T_e is reduced, and all theories find increasing sensitivity with the product of T_e and T_i. Non-dimensional ratios used above are given as: pressure: $\beta \propto PB_T^{-2} \propto n_eT_e$, collisionality: $\nu_* \propto n_e\eta_{||}T_e^{-\frac{1}{2}} \propto n_eT_e^{-2}$, gyro-radius: $\rho_* \propto T_i^{\frac{1}{2}}B_T^{-1} \propto T_i^{\frac{1}{2}}$, where the final proportionality is purely to kinetic parameters (n_e,T_e,T_i).

A. Existing EF penetration scaling laws

The most conventional interpretation for the observations above can be found by considering the existing scaling laws for standard EF penetration in Ohmic plasmas through loss of torque balance. This canonical problem has received much theoretical attention, with many scaling relationships developed progressively including more physical effects.[8–12] While the detailed physics of each model are outside the scope of this work, Table I summarizes the scaling dependence on T_e and T_eT_i, which are the proposed channel for instability as $I_{\rm RE}$ grows and T_e drops. While no T_i measurements are available, it is logical to assume it drops alongside T_e due to the drop in Ohmic input power. Considering T_e alone (4th column in Tab. I), the most inclusive models predict increased sensitivity as T_e drops. Some, such as Ref. 12 predict very strong (cubic) scaling, indicating very minor changes in T_e could have a significant impact. When including both T_e and T_i all models find increased sensitivity to the residual EF as temperatures drop. Thus, while other mechanisms are possible, simply considering the scaling with T_e and T_i of existing theories for EF penetration are consistent with the observation of increased sensitivity to EF penetration. While a residual n=1 EF is necessary, it could be vanishingly small yet still allow EF penetration at finite density due to the impact of the REs. It also bears repeating that the rotating onset observed in Fig. 8 does not preclude a standard EF penetration mechanism, due to the non-axisymmetry (effective 'error field') introduced by the sawtooth post-cursor oscillations.

B. Classical instability

As $I_{\rm RE}$ approaches $I_{\rm tot}$, an intuitive suggestion for instability onset might be modifications to the classical tearing stability index Δ' due to the different current profile (presumably more peaked) with significant $I_{\rm RE}$.[31] Previous work found that the linear properties of the classical tearing mode are essentially determined by the thermal plasma, and linear stability is approximately the same as in a plasma without REs but with the same current profile.[32]

Unfortunately, internal measurements of the current profile are not possible in these conditions, as the heating beam used for motional stark effect (MSE) measurements fuels the discharge, overwhelms the ohmic heating power, and compromises RE emission measurements. However, no measurable change in internal inductance (ℓ_i) is observed in these plasmas - both on the long time scale of the gradual HXR growth and the prompt time scale of the ECE rise. This surprising result suggests the current profile with REs is not dramatically different, perhaps because the sawtooth instability still clamps the core q to around 1, redistributing both RE and thermal current alike.[33] While this mechanism cannot be discounted, there is not yet any evidence to support it.

C. Thermo-resistive instability

The drop in Ohmic power is suggestive of another path to tearing instability, namely the recently discovered thermo-resistive mechanism.[34–36] This mechanism essentially requires that Ohmic input power be exceeded by radiative power loss inside a tiny seed island, which then is non-linearly destabilized. This mechanism also requires high ℓ_i, which is satisfied for these discharges ($\ell_i \approx 1.6$). Increasing RE content provides both a decrease in Ohmic power as discussed in Sec. V and also an increase in radiative power loss through cyclotron and synchrotron emission. Power balance analysis is complicated however by the directional nature of the synchrotron emission, which prevents accurate accounting of radiative power with typical diagnostics. Analysis is also complicated by the fact that REs can be confined within magnetic islands,[37] which may amplify effects within the small seed island as compared to the surrounding thermal plasma, hindering diagnosis.

D. Pressure anisotropy (Firehose-type) instability

The pressure anisotropy observed in Fig. 6(d) also reaches a consistent ('critical') level prior to instability onset, coincident with the other observations in Sec. IV. This is suggestive of a firehose-type instability,[38,39] where in a homogenous plasma treatment instability is found at a critical anisotropic pressure, given by $\beta_{||} - \beta_\perp > 2$. However, measurements discussed in Section IV constrain the global β anisotropy to be far below this level, with for example $(\beta_{||} - \beta_\perp) \approx 0.05\%$ from Fig. 5(c). An increased β anisotropy could result if the RE beam is more localized to the plasma core and thus occupies a smaller volume. For example, a centered RE beam of

0.25 m minor radius would have 10x smaller volume than the entire plasma, and thus a much larger β anisotropy - but still well below the homogeneous plasma firehose limit. It is not known if the firehose instability criterion is significantly different in toroidal geometry, nor if other possible pressure anisotropy instabilities may be playing a role in these plasmas. Admittedly, the emission shape changes shown in Fig. 7 are suggestive of this sort of effect. Some general work exists on the effect of anisotropic pressure[40–42] on tokamak equilibrium and stability, which may form a starting point for future stability calculations. Other work has also identified distinct RE-driven MHD instabilities,[43–45] though phenomenology and equilibrium conditions are unlike those observed here.

VII. SCALING AND EXTRAPOLATION

While the definitive identification of the instability mechanism among aforementioned candidates is not yet achieved, extrapolation of the instability onset condition to future and existing tokamaks (such as ITER) is nevertheless possible by calculating when RE content in low density plasmas becomes appreciable. This is done by combining RE generation rate calculations (Eq. 2) with existing scaling relationships for energy confinement in Ohmic plasmas. A simple 0-D model is developed to perform this extrapolation, described below. While crude, the model only requires the most basic tokamak input parameters: plasma current (I_p), toroidal field (B_T), major radius (R), minor radius (a), elongation (κ), and effective charge (Z_{eff}).

The 0-D model calculates for an arbitrary Ohmic tokamak the density at which the Dreicer generation rate, Eq. 2, equals a significant fraction (10%, say) of bulk n_e. Avalanche is ignored for simplicity. Equation 2 depends on the kinetic parameters n_e, T_e, V_{loop}, and Z_{eff}. Calculation inputs are n_e and Z_{eff}. To solve for T_e and V_{loop}, scaling relationships for the energy confinement time and an approximate tokamak resistivity will be used. Power balance yields one relationship between T_e and V_{loop} (assuming all input power is Ohmic), while Ohm's law yields a second relationship between T_e and V_{loop}.

The first relationship is given by power balance in an Ohmic tokamak. Assuming negligible radiative losses, this is given by:

$$\tau_E I_p V_{\text{loop}} = \frac{3}{2} V \langle e T_e n_e \rangle \tag{3}$$

where $V \approx 2\pi^2 a^2 \kappa R$ is the plasma volume, and τ_E is the energy confinement time. The confinement regime of a low density Ohmic tokamak is well described by the neo-alcator energy confinement scaling law:[46,47]

$$\begin{aligned} \tau_E &= 1.03 \times 10^{-21} q^{0.5} n_e^{1.0} a^{1.04} R^{2.04} \\ \tau_E &\approx 10^{-21} \sqrt{q} n_e a R^2 \end{aligned} \tag{4}$$

Where q is the safety factor taken here as the straight tokamak approximation: $q = \frac{2\pi}{\mu_0} \frac{a^2 \kappa B_T}{R I_P}$.[48] Crucially, the linear dependence of τ_E on n_e allows cancellation of n_e in Eq. 3, allowing it to be re-written as a simple expression for T_e in terms of V_{loop}, for input machine parameters described above:

$$T_e = \left[\left(\frac{10^{-21}\sqrt{2}}{3\pi^{\frac{3}{2}} e \sqrt{\mu_0}} \right) \sqrt{\frac{I_p B_T R}{\kappa}} \right] V_{\text{loop}} \tag{5}$$

The second relationship between T_e and V_{loop}, the Ohm's law, requires approximate evaluation of the resistivity. Profile effects are ignored in this 0-D calculation. The Spitzer resistivity $\eta_{\text{sp}} = \gamma_{\text{sp}} T_e^{-1.5}$, where $\gamma_{\text{sp}} = (Z\pi e^2 m_e^{0.5} \ln\Lambda)/(4\pi\epsilon_0)^2$, must be corrected by a few factors, explained in Ref. 49:

$$\eta_{\text{tot}} = \eta_{\text{sp}} f_{\text{CL}} f_{\text{NC}} \tag{6}$$

Where f_{CL} is a classical correction for Z_{eff}, given as: $f_{\text{CL}} = (1 + 1.2Z + 0.22Z^2)/(1 + 3Z + 0.75Z^2)$, and f_{NC} is a neo-classical correction dependent on the aspect ratio, given as: $f_{\text{NC}} \approx \left(1 - \sqrt{\frac{2\epsilon_G}{1+\epsilon_G}}\right)^{-1}$, where $\epsilon_G = a/R$ is the aspect ratio. The expression for f_{NC} is taken in the low collisionality limit, which removes correction terms proportional to the electron collision rate divided by the bounce frequency. The 0-D resistivity estimate can be used to calculate V_{loop}, taking the plasma as a wire of length $2\pi R$ and area $\pi a^2 \kappa$:

$$\begin{aligned} V_{\text{loop}} &= I_p \tfrac{2R}{a^2\kappa} \eta_{\text{tot}} \\ V_{\text{loop}} &= \left(I_p \gamma_{\text{sp}} f_{CL} f_{NC} \tfrac{2R}{a^2\kappa} \right) T_e^{-\frac{3}{2}} \end{aligned} \tag{7}$$

This equation depends only on Z_{eff}, a, R, κ, and is again independent of n_e. Together, Eqs. 5 and 7 yield a system of equations to uniquely solve for T_e and V_{loop}. Treating n_e as a free parameter, and inserting the input parameters I_p, B_T, a, κ, R, Z_{eff}, as well as the calculated T_e and V_{loop}, the Dreicer generation rate (Eq. 2) can be calculated, and normalized to n_e. This gives a fractional volumetric production rate per second, and the n_e corresponding to a 0.1/s production is taken as the critical value. The sharpness of the n_e dependence results in relative insensitivity to the chosen critical value.

This computation is presented in Fig. 11(a) for a variety of tokamak parameters, taken from Sec. 11.23 in Ref. 50, including the ITER tokamak currently under construction. This calculation indicates that the critical n_e for robust RE production decreases as machine size increases, with a very low critical density predicted for ITER in particular. The scaling with machine size is explored directly in Fig. 11(b), where nominal ITER parameters are scaled down by self-similarly scaling R, a, ${I_p}^2$, and B_T together. This scaling maintains I_p/aB_T and aspect ratio, simulating the overall effect of reducing tokamak size. This calculation reproduces the previous result that as machine size is increased the critical n_e decreases. While the 0-D model developed is basic, the scaling is sufficiently strong that this effect appears very

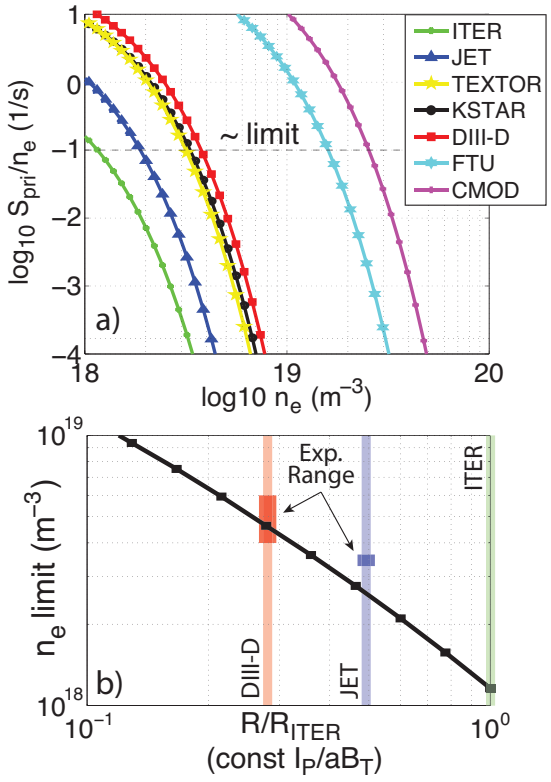

FIG. 11. (a) Volumetric Dreicer production rate normalized by n_e vs n_e itself for typical parameters from many devices, indicating the n_e at which significant REs are produced is separated in machine size. (b) Scaling R, a, B_T, $I_p{}^2$ together from the ITER design point recovers the same trend, with $R/R_{\rm ITER}$ shown for a DIII-D and JET, along with the experimental n_e range where penetration is observed.

unlikely to be encountered in normal ITER operational conditions and is consistent with the reduced density at penetration in JET (Fig. 2) compared to DIII-D.

In addition to the 0-D model for evaluation of $S_{\rm pri}$ (Eq. 2), which is a complicated function, intuition can be gained by noting its dominant sensitivity is to E/E_D, the ratio of the toroidal electric field to the Dreicer field (Eq. 1). Equations 5 and 7 can also be used to identify the scaling E/E_D with machine parameters, giving a simpler, but cruder scaling relationship:

$$\frac{E}{E_D} = \frac{1}{n_e}\frac{2\varepsilon_0^2}{e^3\ln\Lambda}\frac{V_{\rm loop}T_e}{R} \propto \frac{1}{n_e}R^{-\frac{3}{10}}a^{-\frac{8}{5}}\kappa^{-\frac{7}{10}}I_p^{\frac{7}{10}}B_T^{-\frac{1}{10}} \quad (8)$$

Scaling with machine size holding constant I_p/aB_T as in Fig. 11(b) ($R \propto a \propto B_T \propto I_P^2$) the net scaling of E/E_D is given by: $n_e^{-1}R^{-\frac{3}{5}}\kappa^{-\frac{7}{10}}$, confirming a weaker effect with larger machine size. However, this scaling is less dramatic than the full 0-D $S_{\rm pri}$ model. For completeness, the scaling with the critical field for avalanche is also presented, though as mentioned RE avalanche is not included in the 0-D model:

$$\frac{E}{E_C} = \frac{1}{n_e}\frac{2\varepsilon_0^2 m_e c^2}{e^3\ln\Lambda}\frac{V_{\rm loop}}{R} \propto \frac{1}{n_e}R^{-\frac{9}{10}}a^{-\frac{4}{5}}\kappa^{-\frac{1}{10}}I_p^{\frac{1}{10}}B_T^{-\frac{3}{10}} \quad (9)$$

Which scales as $n_e^{-1}R^{-\frac{9}{5}}\kappa^{-\frac{1}{10}}$ with the ($R \propto a \propto B_T \propto I_P^2$) scaling. The 0-D model result is thus confirmed in the simple scaling of both critical field ratios; supporting the increasing difficulty of accessing this limit as machine size is increased.

VIII. DISCUSSION AND CONCLUSION

In this work a novel phenomenon setting the tokamak low-density stability limit has been presented. Unlike the standard low-density penetration driven by significant EFs, instability onset is here preceded by non-thermalization of the discharge due to robust RE growth. Repeatable observations indicate that the RE population is significant, and several marked changes are observed prior to penetration. Measurements include significant HXR emission, non-thermalization of the ECE, decrease in $V_{\rm loop}$ and Ohmic heating, and subsequent drop in T_e. Most notably, instability is found at similar levels of RE emission intensity, and instability cannot be avoided by raising the density so long as RE growth still proceeds to the critical level.

Unlike the conventional interpretation of the low-density limit, the stability limit here described does not depend on the level of residual EF. This can be seen by the off-trend appearance of instability in Fig. 4 as well as the rotating onset shown in Fig. 8. It is also worth noting that the discharges of Fig. 9 employed in-vessel n=1 EF correction, while discharges of Fig. 6 employed ex-vessel n=1 EFC. No difference in phenomenology is seen between the two cases, despite the very different correction spectra and thus different n=1 residual EF spectrum. This similarity supports the conclusion that secondary n=1 EF components (i.e., residual n=1 EFs) do not limit low density access.

These results also stand in contrast to the accepted interpretation of low-density access as a metric for EF correction accuracy - at least for the very low densities where RE growth occurs. If conventional EF penetration scaling laws still apply, a better metric for EF correction accuracy at low density may be the tolerable $I_{\rm RE}$ level and T_e drop, as opposed to the density limit itself. Low density and $I_{\rm RE}$ tend to come together through Eq. 2, but this can be decoupled by introducing some gas puffing and waiting for instability, as in Fig. 5. These results also motivate examination of the low-density stability limit in devices with naturally low intrinsic EF, as has been reported in the KSTAR device.[51]

Interestingly, this stability limit is dependent on a time-integral quantity. Said differently, the proximity to the stability limit for a given equilibrium is dependent on

how long one waits. This does not mean, however, that all tokamak discharges are doomed to instability by this mechanism were their pulses infinitely long. This is because REs are also continually lost or dissipated through other mechanisms, as has been shown in recent experiments and theory.[24,26,52–54] Most tokamak discharges operate at higher density where the RE growth is exponentially weaker in magnitude, and cannot overcome RE loss mechanisms.

By developing a scaling law for this phenomenon, it is observed that the density required for robust RE growth is a decreasing function of tokamak size. Thus, the density required for this limit to be accessed in the largest tokamaks, such as JET and ITER, is very low. For ITER, it is outside of the expected operating density range, while for JET the same phenomenon has been observed only at the low-density record for that device. In combination with the experimental scalings of conventional EF penetration, these results indicate that unless ITER is built with an exceptionally small intrinsic EF it is more likely to encounter conventional EF penetration due to inaccurate n=1 EF correction than instability due to the RE effect discussed in this work.

ACKNOWLEDGMENTS

The authors wish to thank N. Ferraro and E.J. Strait useful discussions; N. Commaux and C.M. Cooper for operational support; T. Luce for collaborative support; M. Austin and Y. Zhu for diagnostic support; and X. Lee for computation support. This material is based upon work supported by the U.S. Department of Energy, Office of Science, Office of Fusion Energy Sciences, using the DIII-D National Fusion Facility, a DOE Office of Science user facility, under Award DE-XXXX. This work has been carried out within the framework of the EUROfusion Consortium and has received funding from the Euratom research and training programme 2014-2018 under grant agreement No 633053 and from the RCUK Energy Programme [grant number EP/I501045]. The views and opinions expressed herein do not necessarily reflect those of the European Commission. DIII-D data shown in this paper can be obtained in digital format by following the links at `https://fusion.gat.com/global/D3D_DMP`.

REFERENCES

[1] Scoville J T, La Haye R J, Kellman A G, Osborne T H, Stambaugh R D, Strait E J and Taylor T S 1991 *Nuclear Fusion* **31** 875 URL `http://iopscience.iop.org/0029-5515/31/5/006`

[2] Buttery R J, M D, Gates D A, Gribov Y, Hender T C, La Haye R J, Leahy P, Leuer J A, Morris A W, Santaguistina A, Scoville J T, Tubbing B J D, Team J, Team C D and Team D D 1999 *Nuclear Fusion* **39** 1827 URL `http://iopscience.iop.org/0029-5515/39/11Y/323`

[3] Buttery R J, De'Benedetti M, Hender T C and Tubbing B J D 2000 *Nuclear Fusion* **40** 807 URL `http://iopscience.iop.org/0029-5515/40/4/306`

[4] Wolfe S M, Hutchinson I H, Granetz R S, Rice J E, Hubbard A E, Lynn A, Phillips P, Hender T C, Howell D F, La Haye R J and Scoville J T 2005 *Physics of Plasmas* **12** 056110 ISSN 1070664X URL `http://link.aip.org/link/PHPAEN/v12/i5/p056110/s1&Agg=doi`

[5] Howell D F, Hender T C and Cunningham G 2007 *Nuclear Fusion* **47** 1336–1340 ISSN 0029-5515 URL `http://stacks.iop.org/0029-5515/47/i=9/a=034?key=crossref.65596a56e25a2d000d1b3882b7136f8f`

[6] Menard J E, Bell R E, Gates D A, Gerhardt S P, Park J K, Sabbagh S A, Berkery J W, Egan A, Kallman J, Kaye S M, LeBlanc B P, Liu Y Q, Sontag A C, Swanson D, Yuh H and Zhu W 2010 *Nuclear Fusion* **50** 045008 ISSN 0029-5515 URL `http://stacks.iop.org/0029-5515/50/i=4/a=045008?key=crossref.43fc218fffc2e2c6ab2d8abb15db0b0e`

[7] Strait E J 2015 *Physics of Plasmas* **22** 021803 ISSN 1070-664X URL `http://scitation.aip.org/content/aip/journal/pop/22/2/10.1063/1.4902126`

[8] Fitzpatrick R 1993 *Nuclear Fusion* **33** 1049–1084 ISSN 0029-5515 URL `http://www.iop.org/EJ/abstract/0029-5515/33/7/I08/`

[9] Scoville J T and La Haye R J 2003 *Nuclear Fusion* **43** 250 URL `http://iopscience.iop.org/0029-5515/43/4/305`

[10] Cole A J and Fitzpatrick R 2006 *Physics of Plasmas* **13** 0–9 ISSN 1070664X

[11] Cole A J, Hegna C C and Callen J D 2008 *Physics of Plasmas* **15** 056102 ISSN 1070664X URL `http://link.aip.org/link/PHPAEN/v15/i5/p056102/s1&Agg=doi`

[12] Fitzpatrick R 2012 *Plasma Physics and Controlled Fusion* **54** 094002 ISSN 0741-3335 URL `http://stacks.iop.org/0741-3335/54/i=9/a=094002?key=crossref.86e198ff30c9323b2048ad6e7b5a8071`

[13] Fitzpatrick R 2014 *Physics of Plasmas* **21** 092513 ISSN 1070-664X URL `http://scitation.aip.org/content/aip/journal/pop/21/9/10.1063/1.4896244`

[14] Hender T C, Wesley J C, Bialek J M, Bondeson A, Boozer A H, Buttery R J, Garofalo A M, Goodman T P, Granetz R S, Gribov Y, Gruber O, Gryaznevich M P, Giruzzi G, Günter S, Hayashi N, Helander P, Hegna C C, Howell D F, Humphreys D A, Huysmans G T A, Hyatt A W, Isayama A, Jardin S C, Kawano Y, Kellman A G, Kessel C E, Koslowski H R, LaHaye R J, Lazzaro E, Liu Y Q, Lukash V, Manickam J, Medvedev S, Mertens V, Mirnov S V, Nakamura Y, Navratil G A, Okabayashi M, Ozeki T, Paccagnella R, Pautasso G, Porcelli F, Pustovitov V D, Riccardo V, Sato M, Sauter O, Schaffer M J, Shimada M, Sonato P, Strait E J, Sugihara M, Takechi M, Turnbull A D, Westerhof E, Whyte D G, Yoshino R, Zohm H, Group, the Itpa Mhd D and Magnet 2007 *Nuclear Fusion* **47** S128–S202 ISSN 0029-5515 URL `http://stacks.iop.org/0029-5515/47/i=6/a=S03?key=crossref.0b9322e42a59b955269531e35f39b3bb`

[15] Buttery R J, Boozer A H, Liu Y Q, Park J K, Ferraro N M, Amoskov V, Gribov Y, La Haye R J, Lamzin E, Menard J E, Schaffer M J and Strait E J 2012 *Physics of Plasmas* **19** 056111

[16] La Haye R J, Paz-Soldan C and Strait E J 2015 *Nuclear Fusion* **55** 023011 ISSN 0029-5515 URL `http://stacks.iop.org/0029-5515/55/i=2/a=023011?key=crossref.10e7d4d23d0590f3541aca41ddd253c4`

[17] Park J K, Boozer A H and Glasser A H 2007 *Physics of Plasmas* **14** 052110 ISSN 1070664X URL `http://link.aip.org/link/PHPAEN/v14/i5/p052110/s1&Agg=doi`

[18] Paz-Soldan C, Lanctot M J, Logan N C, Shiraki D, Buttery R J, Hanson J M, La Haye R J, Park J K, Solomon W M and Strait E J 2014 *Physics of Plasmas* **21** 072503 URL `http://dx.doi.org/10.1063/1.4886795`

[19] Dreicer H 1959 *Phys. Rev.* **115** 238–249

[20] Dreicer H 1960 *Phys. Rev.* **117** 329–342

[21] Helander P, Eriksson L G and Andersson F 2002 *Plasma Physics and Controlled Fusion* **44** B247 URL `http://stacks.iop.org/`

0741-3335/44/i=12B/a=318
[22]Greenwald M, Terry J L, Wolfe S M, Ejima S, Bell M G, Kaye S M and Neilson G H 1988 *Nuclear Fusion* **28** 2199–2207 ISSN 0029-5515
[23]Greenwald M 2002 *Plasma Physics and Controlled Fusion* **44** R27 URL http://iopscience.iop.org/0741-3335/44/8/201
[24]Paz-Soldan C, Eidietis N W, Granetz R S, Hollmann E M, Moyer R A, Crocker N A, Wingen A and Zhu Y 2014 *Physics of Plasmas* **21** 022514
[25]Gill R D, Alper B, de Baar M, Hender T C, Johnson M F, Riccardo V and contributors to the EFDA-JET Workprogramme 2002 *Nuclear Fusion* **42** 1039 URL http://stacks.iop.org/0029-5515/42/i=8/a=312
[26]Stahl A, Hirvijoki E, Decker J, Embreus O and Fulop T 2015 *Phys. Rev. Lett.* **114** 115002
[27]Park J K, Schaffer M J, La Haye R J, Scoville J T and Menard J E 2011 *Nuclear Fusion* **51** 023003 ISSN 0029-5515 URL http://stacks.iop.org/0029-5515/51/i=2/a=023003?key=crossref.2eaa2cc8b363dff2e241621a3cc50ac9
[28]Paz-Soldan C, Logan N C, Lanctot M J, Hanson J M, King J D, La Haye R J, Nazikian R, Park J K and Strait E J 2015 *Nuclear Fusion* **55** 083012 ISSN 0029-5515 URL http://stacks.iop.org/0029-5515/55/i=8/a=083012?key=crossref.0c5f094192f51ea8498e94d094d0f91d
[29]Lao L L, St John H and Stambaugh R D 1985 *Nuclear Fusion* **25** 1421
[30]Yu J H, Hollmann E M, Commaux N, Eidietis N W, Humphreys D A, James A N, Jernigan T C and Moyer R A 2013 *Physics of Plasmas* **20** 042113 URL http://link.aip.org/link/?PHPAEN/20/042113/1
[31]Smith H M, Fehér T, Fülöp T, Gál K and Verwichte E 2009 *Plasma Physics and Controlled Fusion* **51** 124008 ISSN 0741-3335 URL http://stacks.iop.org/0741-3335/51/i=12/a=124008?key=crossref.26970a8f8472b71985533175516f5ce0
[32]Helander P, Grasso D, Hastie R J and Perona A 2007 *Physics of Plasmas* **14** 1–9 ISSN 1070664X URL http://dx.doi.org/10.1063/1.2817016
[33]Cai H and Fu G 2015 *Nuclear Fusion* **55** 022001 ISSN 0029-5515 URL http://stacks.iop.org/0029-5515/55/i=2/a=022001?key=crossref.bd9375fd3ddd1c634c8c09910f9bac08
[34]Gates D A and Delgado-Aparicio L 2012 *Physical Review Letters* **108** 1–4 ISSN 0031-9007 URL http://link.aps.org/doi/10.1103/PhysRevLett.108.165004
[35]White R B, Gates D a and Brennan D P 2015 *Physics of Plasmas* **22** 022514 ISSN 1070-664X URL http://scitation.aip.org/content/aip/journal/pop/22/2/10.1063/1.4913433
[36]Gates D A, Brennan D P, Delgado-Aparicio L and White R B 2015 *Physics of Plasmas* **22** 060701 ISSN 1070-664X URL http://scitation.aip.org/content/aip/journal/pop/22/6/10.1063/1.4922472
[37]Jaspers R, Cardozo N and Finken K H 1994 *Physical Review Letters* **72** 4093–4097 URL http://link.aps.org/doi/10.1103/PhysRevLett.72.4093
[38]Parker E N 1958 *Physical Review* **109** 1874–1876 ISSN 0031899X
[39]Noerdlinger P D and Yui A K M 1968 *Astrophysical Journal* **151** 901
[40]Bishop C and Hastie R 1985 *Nuclear Fusion* **25** 1443–1449 ISSN 0029-5515
[41]Qu Z S, Fitzgerald M and Hole M J 2014 *Plasma Physics and Controlled Fusion* **56** 075007 ISSN 0741-3335 (*Preprint* arXiv:1401.5520v1) URL http://stacks.iop.org/0741-3335/56/i=7/a=075007?key=crossref.b7845bc8eadfeea441e5d4411108695d
[42]Fitzgerald M, Hole M J and Qu Z S 2015 *Plasma Physics and Controlled Fusion* **57** 025018 ISSN 0741-3335 URL http://stacks.iop.org/0741-3335/57/i=2/a=025018?key=crossref.cf1f1710e697d17324506ac62dac88d2
[43]Zonca F, Buratti P, Cardinali A, Chen L, Dong J Q, Long Y X, Milovanov A V, Romanelli F, Smeulders P, Wang L, Wang Z T, Castaldo C, Cesario R, Giovannozzi E, Marinucci M and Ridolfini V P 2007 *Nuclear Fusion* **47** 1588 ISSN 0029-5515 (*Preprint* 0707.2852) URL http://arxiv.org/abs/0707.2852
[44]Delgado-Aparicio L, Sugiyama L, Shiraiwa S, Irby J, Granetz R, Parker R, Baek S G, Faust I, Wallace G, Gates D a, Gorelenkov N N, Mumgaard R, Scott S, Bertelli N, Gao C, Greenwald M, Hubbard a, Hughes J, Marmar E, Phillips P E, Rice J E, Rowan W L, Wilson R, Wolfe S and Wukitch S 2015 *Physics of Plasmas* **22** 050701 ISSN 1070-664X URL http://scitation.aip.org/content/aip/journal/pop/22/5/10.1063/1.4919964
[45]Zhou R J, Hu L Q, Li E Z, Xu M, Zhong G Q, Xu L Q, Lin S Y and Zhang J Z 2013 *Plasma Physics and Controlled Fusion* **55** 055006 ISSN 0741-3335 URL http://stacks.iop.org/0741-3335/55/i=5/a=055006?key=crossref.3b6a8e547b3954be32aeb26d9722aa69
[46]Pfeiffer W and Waltz R E 1979 *Nuclear Fusion* **19** 51 URL http://stacks.iop.org/0029-5515/19/i=1/a=006
[47]Goldston R J 2002 *Plasma Physics and Controlled Fusion* **26** 87–103 ISSN 0741-3335
[48]Freidberg J P 1982 *Reviews of Modern Physics* **54** 801 URL http://link.aps.org/doi/10.1103/RevModPhys.54.801http://rmp.aps.org/abstract/RMP/v54/i3/p801_1
[49]Zarnstorff M C, McGuire K, Bell M G, Grek B, Johnson D, McCune D, Park H, Ramsey a and Taylor G 1990 *Physics of Fluids B: Plasma Physics* **2** 1852 ISSN 08998221 URL http://scitation.aip.org/content/aip/journal/pofb/2/8/10.1063/1.859456
[50]Wesson J A 1987 *Tokamaks* 1st ed (Oxford: Oxford University Press) ISBN 0198563280
[51]In Y, Park J K, Jeon J M, Kim J and Okabayashi M 2015 *Nuclear Fusion* 043004
[52]Granetz R S, Esposito B, Kim J H, Koslowski R, Lehnen M, Martin-Solis J R, Paz-Soldan C, Rhee T, Wesley J C, Zeng L and Group I M 2014 *Physics of Plasmas* **21** 072506 URL http://dx.doi.org/10.1063/1.4886802
[53]Hollmann E M, Parks P B, Commaux N, Eidietis N W, Moyer R A, Shiraki D, Austin M E, Lasnier C J, Paz-Soldan C and Rudakov D L 2015 *Physics of Plasmas* **22** 056108
[54]Aleynikov P B and Breizman B N 2015 *Physical Review Letters* **114** 155001 ISSN 0031-9007 URL http://link.aps.org/doi/10.1103/PhysRevLett.114.155001